Supramolecular Photocatalysts Hot Paper

How to cite: *Angew. Chem. Int. Ed.* **2022,** *61,* e202214055
International Edition: doi.org/10.1002/anie.202214055
German Edition: doi.org/10.1002/ange.202214055

Assembling Phenothiazine into a Porous Coordination Cage to Improve Its Photocatalytic Efficiency for Organic Transformations

Hengyu Lin[+], Zhifeng Xiao, Khoa N. Le, Tian-hao Yan, Peiyu Cai, Yihao Yang, Gregory S. Day, Hannah F. Drake, Haomiao Xie, Riya Bose, Conor A. Ryan, Christopher H. Hendon, and Hong-Cai Zhou**

Abstract: Photo-catalysis by small-molecules is often limited by catalyst degradation and low electron-transfer efficiency. Herein we report a stable N-phenyl-phenothiazine (PTH)-derived porous coordination cage (PCC) as a highly efficient photocatalyst. By the incorporation of the photocatalytic PTH moiety into a PCC, aggregation-induced quenching (AIQ) was shown to be reduced. An improvement in catalyst stability was discovered, ascribed to the synergistic effects of the PTH moieties. The catalyst, operating through a photolytic single-electron transfer, was utilized for photo-catalyzed dehalogenation and borylation. Evaluation of the catalytic mechanism in the borylation reaction showed that the improved performance results from the more efficient formation of the electron donor-acceptor (EDA) complex with the cage. This discovery provides a potential strategy to improve the photophysical properties and stabilities of small-molecule organic photocatalysts via supramolecular chemistry.

Introduction

Photoredox catalysis harvests electromagnetic energy of the incident photon flux to catalyze electron transfer reactions.[1–3] The involvement of light during the catalysis facilitates desirable reactions under mild conditions and through efficient catalytic cycles.[4] For example, borylation of aryl chlorides was traditionally achieved with palladium complex catalysts at 110 °C under air free conditions, while similar conversion using a photocatalyst can be achieved at room temperature with an LED light.[5–7] These fascinating chemistries are rendered by photocatalysts that can initiate photoinduced electron transfer (PET). The photoexcited photocatalysts (PCs) act as potent redox reagents that initiate the bond cleavage and/or redox reactions in the first step of the catalytic cycle. Especially, organic PCs, have high redox potential and broad structural diversity that allows for on-demand molecular design. N-phenylphenothiazine (PTH), belonging to an emerging class of organic PCs, has a high reduction potential of −2.3 V in its excited state, representing a comparable reducibility to that of elemental sodium. Owing to the potent reducibility upon excitation, PTH was reportedly utilized in photocatalytic atom transfer radical polymerization reactions as well as various bond formation reactions, including C–C, C–H, and C–O bonds.[8–15] However, PTH and its derivatives, together with many other organic PCs, suffer from some common detrimental issues, such as low turnover number and relatively long reaction time, due to the short exciton lifetime and poor stability against photobleaching.[16]

Porous coordination cages (PCCs), also known as metal-organic polyhedra (MOPs), are nanoscale cage-like compounds assembled from organic linkers and metal clusters through coordination bonds.[17–20] PCCs can be solubilized in appropriate solvents while maintaining cage-like structures with internal cavities for guest binding.[21] Through rational structural design, the properties of PCCs, including charge, size, geometry and guest affinity, can be adjusted towards targeted functions of the designed PCCs. Particularly, PCCs have been widely utilized as nanoscale reactors to catalyze intermolecular reactions.[22–38] The highly tunable nature of PCC structures allows for customization towards high reactivity for a reaction of interest. For instance, charge, hydrophobicity, and size of a PCC can be tuned by rational design to achieve strong and specific binding towards the reactants of interest. To the best of our knowledge, research on photocatalytic PCCs remains preliminary so far, with most work focusing on photodegradation and photoinduced hydrogen evolution reaction (HER).[39,40]

We envisioned the implementation of a photocatalytic organic moiety into a PCC can generate a PCC-based homogeneous photocatalysts with improved catalytic performance compared to the starting organic PC. The integration of an organic PC into the linker of a PCC can constrain molecular configuration of the photoactive moiety upon

[*] H. Lin,[+] Z. Xiao, T.-h. Yan, Dr. P. Cai, Y. Yang, Dr. G. S. Day, Dr. H. F. Drake, Dr. H. Xie, Prof. H.-C. Zhou
Department of Chemistry, Texas A&M University
College Station, TX 77843 (USA)
E-mail: zhou@chem.tamu.edu

K. N. Le, Prof. C. H. Hendon
Department of Chemistry, University of Oregon
Eugene, OR 97403 (USA)
E-mail: chendon@uoregon.edu

R. Bose, C. A. Ryan
Department of Physics, University of Texas at Dallas
800 W. Campbell Rd., Richardson, TX 75080 (USA)

[+] These authors contributed equally to this work.

excitation, which can potentially stabilize the organic PC and deter photobleaching. Preorganization effect from the PCC assembling can combine multiple photocatalytic cores into a singular cage and facilitate optimal substrate binding, which might allow for more efficient SET during the initiation of the photocatalytic cycle. In this work, we aim to design and synthesize a PCC-based photocatalyst and characterize its photocatalytic performance systematically to validate the strategy. To ensure the stability of the targeted PCC during photocatalysis, a zirconocene-based cluster, $[Zr_3Cp_3(\mu_2\text{-}OH)_3(\mu_3\text{-}O)]$ (ZrCp),[41] was utilized in a [4+4] reaction to construct a tetrahedral PCC with a PTH-derived tricarboxylate linker, $\mathbf{L1}^{3-}$ (Figure 1a). The ZrCp cluster has C_3-symmetry and form robust Zr–O bonds with the tricarboxylate linkers. With tricarboxylate linker of 3-fold symmetry, the ZrCp cluster can form positively charged tetrahedral PCCs possessing superior stability under acidic and weakly alkaline conditions. The ZrCp-based PCCs have gained broad interests due to their structural diversity and outstanding performance in various applications, including sensing, homogeneous catalysis,[42–44] separation,[45] antimicrobial therapy,[46] and bioimaging.[47] Herein, we report the construction of a new ZrCp-based tetrahedral PCC, PCC-40, with a photocatalytic organic linker $\mathbf{L1}^{3-}$, derived from 3,7-di(p-carboxylic)-N-(p-phenylcarboxylic)-phenothiazine (H_3**L1**), and the photocatalytic performance in various reactions of cage.

Results and Discussion

Recently, Yuan and co-workers used a triphenyl amine-based ligand (H_3TCPA) to construct a similar PCC (**Zr-MOC-1**) with the **ZrCp** cluster.[48] Through rational structural design, $\mathbf{L1}^{3-}$ can form a tetrahedral PCC (**PCC-40**) with the $[(ZrCp)_4(\mathbf{L1})_4]^{4+}$ cluster (Figure S3a).Our numerous attempts in determining the crystal structure of **PCC-40** via single crystal X-ray diffraction (SCXRD) were unsuccessful, because of the overall weak diffractions and the lack of diffraction spots at the high angle region, presumably due to the high solvent-accessible volume and the random packing of the PCCs in the lattice. Upon modelling based on the PXRD patterns, **PCC-40** was found to share the similar peak pattern as the simulated structure (Figure S6). The packing among various ZrCp-based cages is highly tunable by weak inter-cage interactions such as hydrogen bonding confirmed by multiple findings.

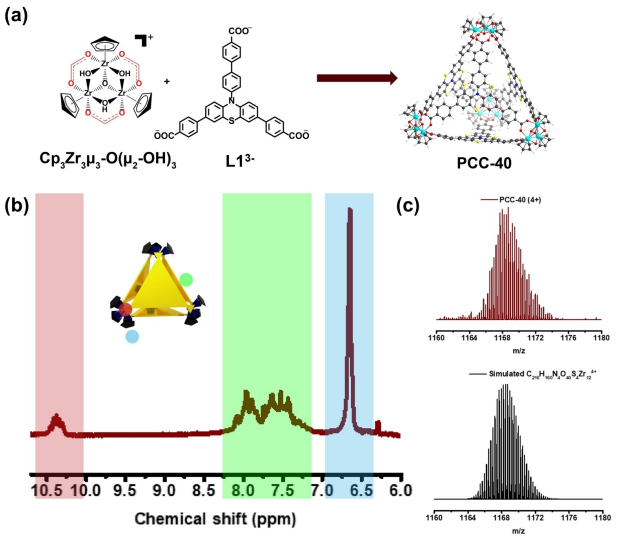

Figure 1. a) The formation of **PCC-40**. b) ^{1}H NMR of **PCC-40** in dmso-d_6. c) ESI-MS of **PCC-40**(4+) and simulated peaks.

The identity of **PCC-40** in solution was confirmed by mass spectrometry and NMR spectroscopic analysis. In the mass spectra of **PCC-40**, multiple positively charged peak envelopes were detected (Figure 1c and S1). They correspond to the **PCC-40** cages of different charges that are presumably generated by the μ^2-OH deprotonation on the clusters. Interestingly, peak envelopes corresponding to **PCC-40** cages with DMA molecules were also found in the mass spectra, indicative of DMA staying with **PCC-40**. In the ^{1}H NMR spectra of **PCC-40** in DMSO-d_6, the protons on the clusters are well-defined (red) and can be assigned to specific chemical shifts, while the protons on the ligands exhibit broad peaks (green) potentially due to the low symmetry of the ligand (Figure 1b), and Cp protons are indicated by blue shade. Two-dimensional (2D) NMR studies on **PCC-40** in solution further verified the cage structure of **PCC-40** is maintained in the solution (Figure S2). The solution state characterization of **PCC-40** supports its potential to be a homogeneous catalyst.

The composition of the **PCC-40** crystals was furthered evidenced by EDS mapping, as colocalization of Zr, C, O, S and Cl throughout the crystals were found in the SEM images (Figure S3b,c). Moreover, the solid-state NMR studies on the **PCC-40** crystals revealed that freely rotating liquid-like DMA molecules existed in the crystal lattice, as evidenced by the relatively sharp proton peaks of DMA at elevated temperatures, which corroborates well with the porous nature of the **PCC-40** crystals (Figure 2). Upon the assemblage of PCCs, the electronic structures of the cages often deviate from the ligands due to the ligand-metal charge transfer (LMCT) and the restrained ligand configuration in the PCC. To investigate the changes in electronic structures, we examined the UV/Visible spectra of the **PCC-40** in DMSO (Figure 3a and Table 1). In the low wavelength region of the UV/Vis spectra (below 350 nm), the sharp absorption peak of **PCC-40** blue shifted compared to the protonated ligand, H_3**L1**, potentially due to the cyclopentadienyl groups on the cluster. While in the visible region (above 350 nm), both **PCC-40** and H_3**L1** exhibit broad absorption at 350–450 nm with **PCC-40** being 10-nm red-shifted compared to H_3**L1**. Quantitative measurements indicated **PCC-40** has an extinction coefficient of 1.36×10^4 cm mL mol^{-1} cm^{-1} at 450 nm, which is 6 times higher than that of H_3**L1** at 440 nm. It should be noted that one **PCC-40** structure contains four H_3**L1** units, albeit the higher than 4-fold increase indicates that the synergistic effect of cage assemblage leads to non-linear enhancement represented by the Beer–Lambert's Law. The increase in extinction coef-

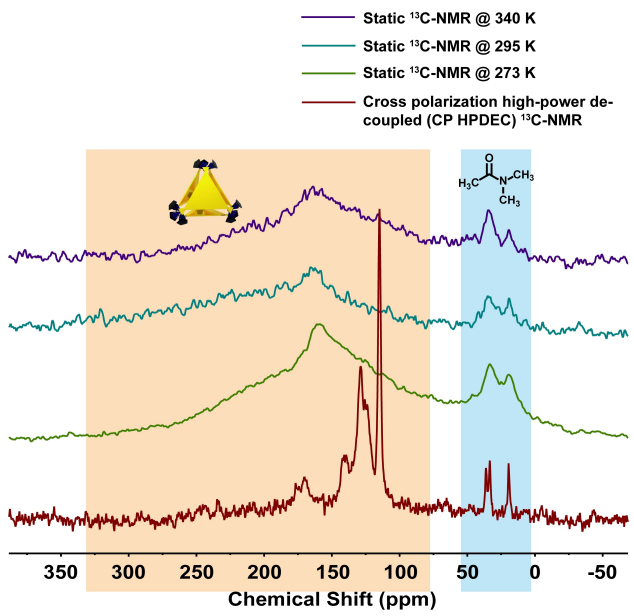

Figure 2. Solid-state ^{13}C NMR of **PCC-40**.

ficient also implies that **PCC-40** can harvest visible light more effectively than its building blocks.

In order to understand how the LMCT affects the photoluminescence properties, the 3D excitation-emission matrix (EEM) spectra of **PTH**, H_3**L1**, and **PCC-40** were measured and compared in Figure 3b–d. Under low wavelength excitation (350 nm), both the ligand H_3**L1** and **PCC-40** exhibit a 450-nm emission peak and secondary emission peaks with longer wavelength. The secondary emission peak for H_3**L1** is located at 535 nm while the one for **PCC-40** is redshifted to 585 nm. The relatively large redshift in the emission spectra strongly implies the prominent change in the electronic structure of the ligand chromophore. To further investigate how cage assembling affects the electronic structure of the chromophore, DFT calculations were carried out to geometrically optimize the structure and compute the molecular orbitals of **PCC-40**. As shown in the optimized **PCC-40** structure (Figure 4), the orientations of the phenyl carboxylates are in-plane with the Zr atoms, which facilitated charge-transfer between the ligand and metal centers. As for the ligand overall configuration, $\mathbf{L1}^{3-}$ in the optimized cage structure exhibit a different configuration than that of H_3**L1** in solution due to the constrained cage structure. Notably, such difference in the ligand configuration results in 14.5 kJ mol^{-1} increase in free energy for each ligand, meaning that the assembling of **PCC-40** distorted the ligand towards an unfavorable configuration. The energy increase resulted from this presumably leads to higher catalytic activities.

The availability of excited states of a PC under light is crucial to its catalytic performance since electron transfer in the initiation of the catalytic cycle takes place between the

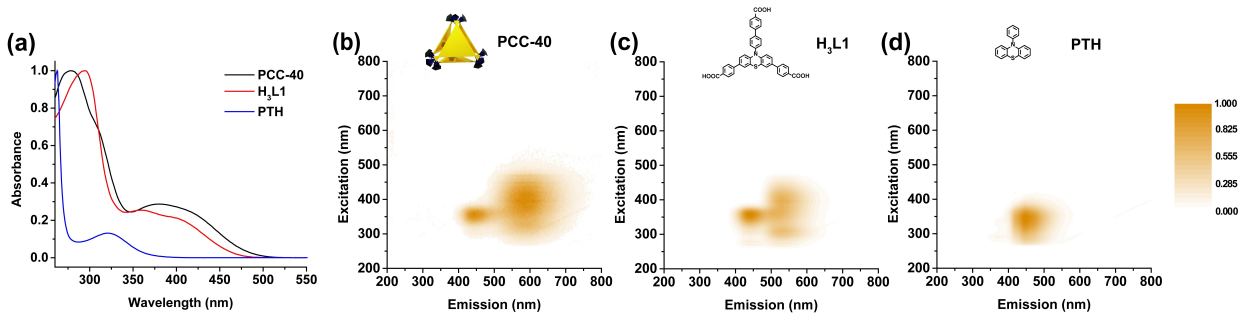

Figure 3. a) UV/Visible absorption spectra of PCC-40, H_3L1, and PTH. b) 3D fluorescence spectrum of **PCC-40**. Horizontal: emission, vertical: excitation. Contour map peak (ex 350 nm, em 450 nm; ex 400 nm, em 585 nm) c) 3D fluorescence spectrum of H_3**L1**. Horizontal: emission, vertical: excitation. Contour map peak (ex 350 nm, em 450 nm; ex 400 nm, em 535 nm) d) 3D fluorescence spectrum of **PTH**. Horizontal: emission, vertical: excitation. Contour map peak (ex 350 nm, em 450 nm).

Table 1: Extinction coefficients of **PCC-40**, H_3**L1**, and **PTH**. ε_{lm} is calculated based on the local absorption maximum with wavelengths longer than 300 nm, that is, 382 nm for **PCC-40**, 360 nm for H_3**L1**, 321 nm for **PTH**. ε_{460} is calculated based on the absorbance at 460 nm. Lifetimes are collected @ 350 nm laser light excitation.

Photocatalyst	ε_{max} / mL·mol^{-1}·cm^{-1}	ε_{460} / mL·mol^{-1}·cm^{-1}	Quantum Yield	FL Weight and Lifetime (A_1, τ_1, A_2, τ_2)
PCC-40	7.42×10^4	1.36×10^4	0.333	@ 585 nm, 0.46, 1.83 ns, 0.47, 3.58 ns $\bar{\tau}$ = 1.40 ns
H_3**L1**	1.30×10^4	1.53×10^3	0.181	@ 535 nm, 0.55, 0.82 ns, 0.40, 3.24 ns $\bar{\tau}$ = 1.08 ns
PTH	4.27×10^3	NA	0.034	@ 450 nm, 0.48, 1.56 ns, 0.44, 4.75 ns $\bar{\tau}$ = 1.74 ns

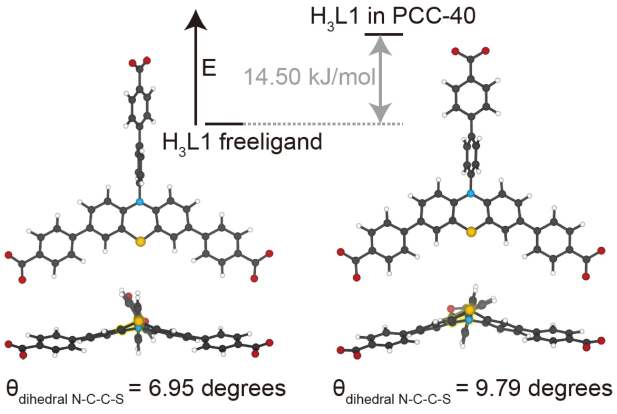

Figure 4. The simulated molecular conformation of free ligand H_3**L1** and H_3**L1** in **PCC-40**. An energy difference of 14.50 kJ mol^{-1} is calculated.

PC at its excited state and the substrate. PCs with higher quantum yields and longer lifetimes are thereby more favorable. Compared to **PTH**, H_3**L1** has seen a dramatic increase in quantum yield from 0.034 to 0.181. As shown in our studies, **PCC-40** has a quantum yield of 0.333 in DMSO. The increase of quantum yield might be caused by rigidification of the ligand in the cage structure. The constrained configuration can, to some extent, eliminate bond rotations that trigger vibronically coupled non-radiative relaxation pathways. Photoluminescence lifetime studies conducted on **PCC-40** and H_3**L1** in the solution revealed a bi-exponential fluorescence decay pathway in both **PCC-40** and H_3**L1** with resembling weights (Figure S9–11, Table 1). It is noteworthy that slightly longer fluorescence lifetimes were observed in **PCC-40** compared to H_3**L1**, which further implied **PCC-40** should have higher photocatalytic efficiency.[4] Meanwhile, aggregation-induced emission/quenching (AIE/AIQ) was studied in the Supporting Information section 8 (Figure S12) to prove the cage's strength in reducing the unfavored AIQ effect.

The photophysical properties of **PCC-40** indicated its feasibility to be an efficient photocatalyst. To further investigate the photocatalytic capability of **PCC-40**, the excited state reductive potential of **PCC-40** was characterized through the method provided by the Alaniz group in Supporting Information section 10. Cyclic voltammetry results are shown in Figure S7–8. Numerous studies on **PTH** as a photocatalyst indicated it reduces the substrate at its excited state by a single electron transfer (SET) process.[9,10,49] We assumed, similarly, **PCC-40** at its photo-excited state (**PCC-40***) can also undergo the SET pathway, donating an electron to the substrate, and get oxidized into **PCC-40**$^{\bullet+}$.

The high reductive potential (−2.23 V, −1.59 V at different conditions) of **PCC-40** at its excited state suggests its potential to initiate a wide range of photoredox reactions via SET. Aryl halides can be reduced by accepting an electron from the PC and forming phenyl radical and halide ions. Theoretically, the measured reducibility of **PCC-40*** is sufficiently high for common aryl halides, such as iodobenzene (−1.2 V) and bromobenzene (−1.8 V), though reluctant for chlorobenzene (−2.1 V) and fluorobenzene. Inspired by **PTH**'s reactivity, the activation of alkyl halides, aryl diazonium tetrafluoroborates, and alkyl hydroxy groups reported previously, we hope to evaluate the performance of **PCC-40** by photoinduced hydrodehalogenation reactions.[50–52] Notably, the resultant phenyl radical has the potential to form highly desirable products that are dominantly synthesized through noble metal-catalyzed coupling reactions, such as, Suzuki Coupling (C–C coupling), Miyaura borylation and Buchwald–Hartwig Cross Coupling (C–N coupling).

Based on the findings, we hypothesized **PCC-40** can effectively reduce aryl halides under light via the SET pathway. The efficiency of such process can be characterized by photocatalytic dehalogenation reaction of aryl halides. In the presence of a proton source, the aryl radical intermediate can be converted into a hydrocarbon. Addition of a proper reducing reagent in the reaction system can recover **PCC-40**$^{+}$ into **PCC-40** for a closed catalytic cycle. The dehalogenation of bromobenzene and iodobenzene was tested with triethylamine/formic acid as reductants (Scheme 1). During condition optimization, 460 nm light was found to more effectively induce the proper excited state in **PCC-40** for SET. Under optimized conditions, the yield recorded at 90 min were 63 % (**PCC-40**) and 38 % (H_3**L1**), respectively. **PCC-40** showed a faster reaction rate compared to H_3**L1** from 0–180 min after reaction had been initiated (Figure S16). In the dehalogenation of iodobenzene, **PCC-40** reached the completion of reaction (78 %) in 10 min, while under the same conditions H_3**L1**'s yield was 14 % at 10 min.

To explain the catalytic performance enhancement, synergistic effects of ligands in **PCC-40** were studied. DFT calculation was performed to compare the energetics of the HOMOs and LUMOs of **PTH**, H_3**L1**, and **PCC-40** (Figure 5a). The results show that **PTH** and H_3**L1**'s HOMOs rests on the phenothiazine center and LUMO rests mostly on the *N*-phenyl. In contrast, the LUMO of **PCC-40** involves the $[Cp_3Zr_3\mu_3\text{-}O(\mu_2\text{-}OH)_3]^{4+}$ cluster while the HOMO involves mostly the organic part (mostly the phenothiazine center). This more expanded electronic distribution supports that metal-ligand charge transfer play an important role in

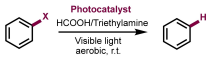

Substrate	Excitation Light	Photocatalyst	Catalyst Loading	Yield @ 90 min	Yield @ 180 min
Bromobenzene	460 nm	PCC-40	0.5%	63%	89%
		H_3L1	0.5%	38%	81%
		PTH	0.5%	1.7%	1.1%
		No catalyst	NA	3.1%	1.6%
				Yield @ 10 min	**Yield @ 30 min**
Iodobenzene	460 nm	PCC-40	0.5%	78%	82%
		H_3L1	0.5%	14%	77%
		PTH	0.5%	0.6%	1.4%
		No catalyst	NA	0.6%	1.3%

Scheme 1. SET-based photocatalytic hydrodehalogenation investigated herein. 460 nm light is applied after condition optimization. Photo-induced hydrodehalogenation of aryl halides (Br and I). Triethylamine is the sacrificial reductive reagent.

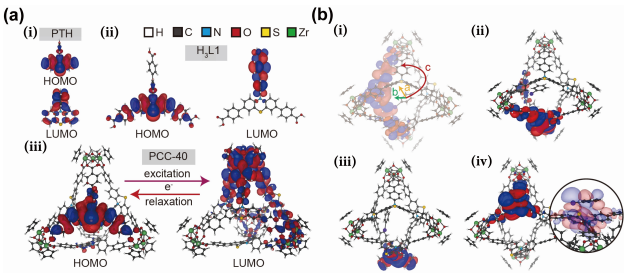

Figure 5. a) DFT calculation on the HOMO, LUMO orbitals of (i) **PTH**; (ii) H_3**L1**; (iii) **PCC-40**. b) HOMO distribution in computational docking of iodobenzene inside/outside **PCC-40**. (i)–(iii) shows stepwise approaching of interior iodobenzene to one H_3**L1** in **PCC-40**. (iv) shows the docking of exterior iodobenzene to one H_3**L1** in **PCC-40**

the catalytic activity of **PCC-40**. Unlike **PTH** and H_3**L1** where the catalytic activity depends solely on the organic component, the involvement of **PCC-40**′s metal clusters in the LUMO explains the shifts of UV/Vis and fluorescence peaks and indicates that the participation of the metal clusters in electron transfer can rationalize the enhanced catalytic rates.

To understand the energy transfer and the synergistic effect of ligands in **PCC-40**, Stern–Volmer fluorescence quenching studies were performed to compare the energy transfer rates of the studied photocatalysts. The quenching coefficients are calculated and listed in Table 2. It is worth mentioning that **PCC-40** with iodobenzene shows enhanced fluorescence under 450 nm excitation light, which has not been reported previously. This effect might be attributed to the host-guest interaction between iodobenzene and **PCC-40**, induced by the confinement effect of the cage, forming an electron donor-acceptor (EDA) complex which shows increased light-absorption. Meanwhile, same level of fluorescence enhancement was not observed when iodobenzene was added to H_3**L1** or **PTH** solution, suggesting that the confinement effect of **PCC-40** assists the photo-induced energy transfer. Computational studies were launched to elaborate the interaction between **PCC-40** and iodobenzene. The docking of an iodobenzene molecule onto **PCC-40** shows that iodobenzene molecules have multiple effects on **PCC-40**′s HOMO dependent on docking positions, including shifting the HOMO to a different organic linker or directly tangling with the HOMO of **PCC-40** (Figure 5b). This complex indicates an electron transfer process from the excited **PCC-40** to iodobenzene, forming an EDA complex under light irradiation. Iodobenzene approaches the **PCC-40** cage and at close enough distance, it actively interacts with the HOMO of **PCC-40**, enhancing its UV absorption, causing enhanced fluorescence. UV/Visible adsorption spectra were collected as incremental amounts of iodobenzene were added to **PCC-40**, H_3**L1**, and **PTH** solutions to substantiate the calculated results (Figure 6). A significant absorbance enhancement @ 425 nm was observed when adding iodobenzene into **PCC-40** solution, while H_3**L1** and **PTH**'s absorbance enhancements were barely observable in the same region. However, **PTH**'s absorbance overlaps with iodobenzene and cannot be observed. These results rationalize the unique phenomenon that fluorescence was enhanced in Stern–Volmer studies, indicating the more efficient formation of EDA complex in solution due to **PCC-40**′s confinement effect on substrates.

Other than synergistic effects, confinement effect from cages were studied with the hypothesis that the quencher molecule can diffuse into and out of the cage and induces an overall slowdown of the diffusion rate of the substrates. Diffusion-ordered spectroscopy DOSY-^{1}H NMR (Figure S25) is utilized to depict the diffusion rates, of which the derived diffusion coefficients are shown in Table 3. A drop in iodobenzene's diffusion coefficient was observed, which to our expectation, is due to the cage's confinement of the substrates.

With the high reactivity of **PCC-40**, it should be noted that C–X activation can be coupled with other reactants to achieve more fascinating coupling reactions. Herein we demonstrated a route to build C–B bonds via the formation of reactive organoboronic acid/ester intermediates. It has been achieved by a range of iridium-based transition-metal complexes yet not accomplished by PTH-based photocatalysts nor by cage catalysts. The fact that both these photocatalysts undergo an SET cycle in C–X bond activation gave us confidence for the test.[6]

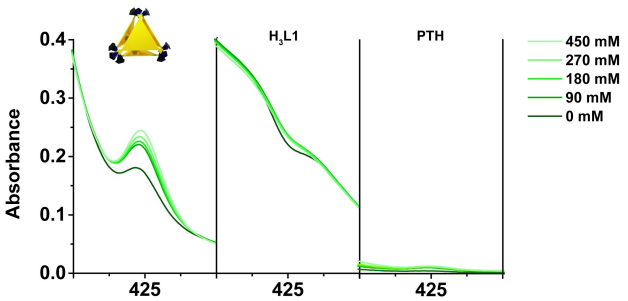

Figure 6. UV/Visible titration of photocatalysts: (i) **PCC-40**; (ii) H_3**L1**; (iii) **PTH**. Different concentrations of iodobenzene are added.

Table 2: Photoluminescence quenching coefficients K_{sv} of **PTH**, H_3**L1**, and **PCC-40** at 450 nm, 535 nm, and 585 nm emissions, respectively. Different emission wavelengths are adopted for max emission intensity. Quenching rate k_q is calculated by average fluorescence lifetime.

Quenching reagent	Catalyst	K_{sv} / M^{-1}	k_q / (ns^{-1} M^{-1})
Iodobenzene	**PTH**	em450, 2.51	1.44
	H_3**L1**	em535, 0.114	0.106
	PCC-40	em585, enhanced fluorescence	Enhanced fluorescence

Table 3: Calculated diffusion coefficients by DOSY-^{1}H NMR with and without the presence of **PCC-40**

Molecule	Diffusion coefficient (10^{-10} m^2/s)	Standard error
Iodobenzene (in DMSO-d_6)	6.3	±0.2
Iodobenzene (in DMSO-d_6 with **PCC-40**)	5.6	±0.1

Herein, condition optimization was launched for photo-borylation, recorded in Supporting Information Section 9. 460 nm excitation for **PCC-40** is greater in yield than 350 nm excitation. A substrate scope of functionalized iodobenzenes was tested (Scheme 2), which revealed that stronger electron-donating groups tend to result in a lower yield and electron-withdrawing groups can enhance the yield. However, a strong electron-withdrawing group, nitro, didn't give an expected high yield, which might be due to the reduction of the nitro group during catalysis rather than the fission of the C–I bond. Also, bromobenzene showed a low catalytic yield, which suggests the applied reaction conditionis barely capable of cleaving the C–Br bond. This might be due to the relatively low concentration of sacrificial reducing reagent used. Another possible factor is the kinetic inhibition of the substrate binding/release under this condition. **PCC-40** shows a higher catalytic yield compared to the H_3**L1** at the same catalyst loading ratio (0.93 %, Scheme 2). Further reducing the catalyst loading ratio, **PCC-40**′s catalytic yields were constantly higher than H_3**L1**′s at each loading ratio tested. Turnover numbers and frequencies were calculated to evaluate the catalyst performance. This suggests that a combinatory set of factors of **PCC-40**′s higher quantum yield (0.333, Table 1), higher quenching rate, synergistic and confinement effects on the substrate (Table 2, Figure 5,6), and elongated catalyst lifetime based on TONs/TOFs calculated in Scheme 2 lead to the better performance of **PCC-40**. Reaction kinetics are shown in Figure S19. Excitation light @ 350 nm showed a lower yield and TON. It is believed that 460 nm light can induce the confinement-involved electron transfer and lead to higher catalytic rates, which was proved by the fluorescence studies (Table 3), structural simulation (Figure 5) and UV/Vis absorption spectra (Figure 6).

The reaction can complete within 4 hours under optimal conditions. Compared to previously reported iridium PCs, there is a remarkable acceleration in catalytic efficiency, with no increase in catalyst loading ratio. Furthermore, the organoboronic acids can be the substrates of multiple C–C, C-heteroatom coupling reactions in one-pot dual-catalysis.

The boron-containing species' transformation pathway is important in the catalytic cycle. ^{1}H NMR was utilized to study the reaction. The disappearance of iodobenzene peaks indicates the complete turnover of the substrate (Figure S18, 20). The proposed mechanism based on ^{1}H NMR and ^{13}B NMR illustrates the SET in the catalytic cycle. **PCC-40** binds with Ar–X to form the EDA complex and gets excited to **PCC-40-ArX*** upon light excitation. The aryl halide accepts an electron from **PCC-40** and labile Ar–X bond cleaves, forming Ar• and X^-, respectively, shown in Scheme 3. Notably, the Ar• formation explains the yields in the substrate scope in Scheme 2 since the radicals are stabilized by electron-withdrawing groups. More details provided in the Supporting Information section 10.

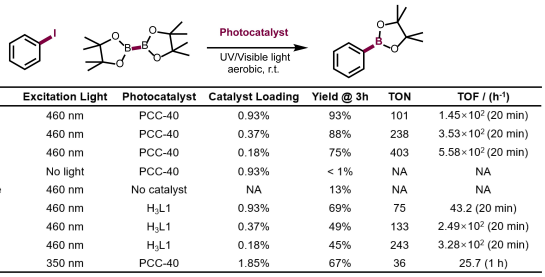

Substrate	Excitation Light	Photocatalyst	Catalyst Loading	Yield @ 3h	TON	TOF / (h^{-1})
	460 nm	PCC-40	0.93%	93%	101	1.45×10^2 (20 min)
	460 nm	PCC-40	0.37%	88%	238	3.53×10^2 (20 min)
	460 nm	PCC-40	0.18%	75%	403	5.58×10^2 (20 min)
	No light	PCC-40	0.93%	< 1%	NA	NA
Iodobenzene	460 nm	No catalyst	NA	13%	NA	NA
	460 nm	H_3L1	0.93%	69%	75	43.2 (20 min)
	460 nm	H_3L1	0.37%	49%	133	2.49×10^2 (20 min)
	460 nm	H_3L1	0.18%	45%	243	3.28×10^2 (20 min)
	350 nm	PCC-40	1.85%	67%	36	25.7 (1 h)

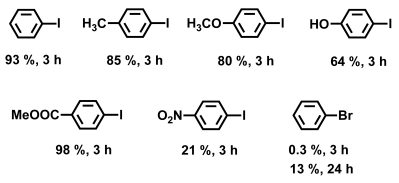

Scheme 2. SET-based photo-borylation of iodobenzene. Sodium ascorbate is the sacrificial reductive reagent. Substrate scope is provided with benzenes functionalized with electron withdrawing/donating groups.

Conclusion

Homogeneous catalysis utilizing porous coordination cages (PCCs) have been widely studied in recent years due to the unique characteristics of PCCs, however, PCCs are rarely composed from organic photocatalytic ligands and utilized as photocatalysts to the best of our knowledge. In summary, this work successfully designed and demonstrated the assembly of **PCC-40**, where for the first time, a photocatalytic core, N-phenyl phenothiazine was incorporated into a [4+4] PCC and utilized as a homogeneous photocatalyst. The assembling of the phenothiazine-containing ligand into **PCC-40** induces changes in the electronic structures of the photocatalytic center and facilitated new substrate–catalyst interactions, which was characterized with spectroscopic techniques and theoretical calculations. Under visible light irradiation, photocatalytic borylation catalyzed by **PCC-40** was characterized and mechanistically studied, with a yield of 93 % starting from iodobenzene within 4 hours, outperforming the counterpart ligand H_3**L1** and **PTH**. The synergistic effect and anti-aggregation effect of

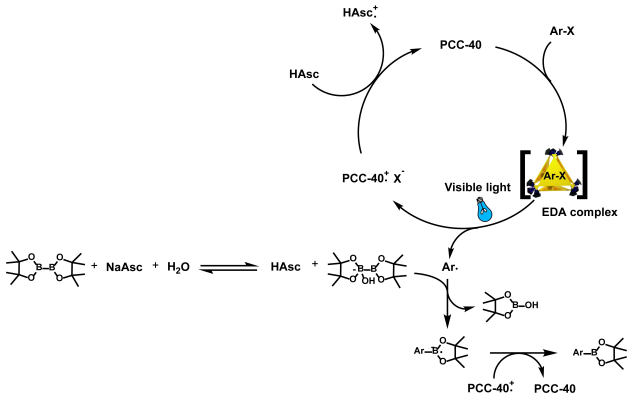

Scheme 3. Proposed reaction mechanism for photo-borylation of catalyzed by **PCC-40**.

the cage assembly were proven to be the key to the outstanding performance observed in our studies. Overall, our present results unambiguously prove the potential of PCCs as a next-generation photocatalyst. The PCC-based photocatalysts may provide alternatives to solve the issues of existing photocatalysts in the literature and play a more important role in organic synthesis.

Acknowledgements

This work is supported by the Robert A. Welch Foundation through a Welch Endowed Chair to H.-C. Z. (A0030) and the National Science Foundation through the Division of Materials Research under grant no. DMR-1956403. This work utilized resources from the Advanced Light Source (ALS), a DOE Office of Science User Facility under contract no. DE-AC02-05CH11231. The ALS beamline 12.2.1 and assistance from Dr. Simon J. Teat are acknowledged. We thank the TAMU Chem NMR Facility, Dr. Gregory P. Wylie, and Dr. Vladimir Bakhmoutov for DOSY 1H NMR and solid-state NMR tests. Use of the Chemistry MASS Spec Facilities by Dr. Yohannes H. Rezenom is acknowledged for acquiring MASS spectrometry data. We pay tribute to TAMU Materials Characterization Core Facility with RRID: SCR_022202. We also would like to thank Prof. Anton Malko for the help in providing photophysical measurements.

Conflict of Interest

The authors declare no conflict of interest.

Data Availability Statement

The data that support the findings of this study are available in the supplementary material of this article.

Keywords: PCC · Photocatalysis · Single-Electron Transfer · Synergistic Effects

[1] D. A. Nagib, D. W. C. MacMillan, *Nature* **2011**, *480*, 224–228.
[2] T. Pirnot Michael, A. Rankic Danica, B. C. Martin David, W. C. MacMillan David, *Science* **2013**, *339*, 1593–1596.
[3] C. K. Prier, D. A. Rankic, D. W. C. MacMillan, *Chem. Rev.* **2013**, *113*, 5322–5363.
[4] N. A. Romero, D. A. Nicewicz, *Chem. Rev.* **2016**, *116*, 10075–10166.
[5] K. L. Billingsley, T. E. Barder, S. L. Buchwald, *Angew. Chem. Int. Ed.* **2007**, *46*, 5359–5363; *Angew. Chem.* **2007**, *119*, 5455–5459.
[6] M. Jiang, H. Yang, H. Fu, *Org. Lett.* **2016**, *18*, 5248–5251.
[7] Y.-M. Tian, X.-N. Guo, H. Braunschweig, U. Radius, T. B. Marder, *Chem. Rev.* **2021**, *121*, 3561–3597.
[8] N. J. Treat, H. Sprafke, J. W. Kramer, P. G. Clark, B. E. Barton, J. Read de Alaniz, B. P. Fors, C. J. Hawker, *J. Am. Chem. Soc.* **2014**, *136*, 16096–16101.
[9] E. H. Discekici, N. J. Treat, S. O. Poelma, K. M. Mattson, Z. M. Hudson, Y. Luo, C. J. Hawker, J. Read de Alaniz, *Chem. Commun.* **2015**, *51*, 11705–11708.
[10] M. H. Aukland, M. Šiaučiulis, A. West, G. J. P. Perry, D. J. Procter, *Nat. Catal.* **2020**, *3*, 163–169.
[11] B. L. Buss, C.-H. Lim, G. M. Miyake, *Angew. Chem. Int. Ed.* **2020**, *59*, 3209–3217; *Angew. Chem.* **2020**, *132*, 3235–3243.
[12] B. G. McCarthy, R. M. Pearson, C.-H. Lim, S. M. Sartor, N. H. Damrauer, G. M. Miyake, *J. Am. Chem. Soc.* **2018**, *140*, 5088–5101.
[13] B. L. Ramsey, R. M. Pearson, L. R. Beck, G. M. Miyake, *Macromolecules* **2017**, *50*, 2668–2674.
[14] C. Theriot Jordan, C.-H. Lim, H. Yang, D. Ryan Matthew, B. Musgrave Charles, M. Miyake Garret, *Science* **2016**, *352*, 1082–1086.
[15] A. Vega-Peñaloza, J. Mateos, X. Companyó, M. Escudero-Casao, L. Dell′Amico, *Angew. Chem. Int. Ed.* **2021**, *60*, 1082–1097; *Angew. Chem.* **2021**, *133*, 1096–1111.
[16] W. Holzer, A. Penzkofer, T. Tsuboi, *Chem. Phys.* **2005**, *308*, 93–102.
[17] E.-S. M. El-Sayed, D. Yuan, *Chem. Lett.* **2020**, *49*, 28–53.
[18] A. J. Gosselin, C. A. Rowland, E. D. Bloch, *Chem. Rev.* **2020**, *120*, 8987–9014.
[19] S. Lee, H. Jeong, D. Nam, M. S. Lah, W. Choe, *Chem. Soc. Rev.* **2021**, *50*, 528–555.
[20] H. Vardhan, M. Yusubov, F. Verpoort, *Coord. Chem. Rev.* **2016**, *306*, 171–194.
[21] M. M. Deegan, A. M. Antonio, G. A. Taggart, E. D. Bloch, *Coord. Chem. Rev.* **2021**, *430*, 213679.
[22] G.-J. Chen, C.-Q. Chen, X.-T. Li, H.-C. Ma, Y.-B. Dong, *Chem. Commun.* **2018**, *54*, 11550–11553.
[23] W. Cullen, M. C. Misuraca, C. A. Hunter, N. H. Williams, M. D. Ward, *Nat. Chem.* **2016**, *8*, 231–236.
[24] Y. Fang, T. Murase, S. Sato, M. Fujita, *J. Am. Chem. Soc.* **2013**, *135*, 613–615.
[25] Y. Fang, J. A. Powell, E. Li, Q. Wang, Z. Perry, A. Kirchon, X. Yang, Z. Xiao, C. Zhu, L. Zhang, F. Huang, H.-C. Zhou, *Chem. Soc. Rev.* **2019**, *48*, 4707–4730.
[26] D. Fiedler, H. van Halbeek, R. G. Bergman, K. N. Raymond, *J. Am. Chem. Soc.* **2006**, *128*, 10240–10252.
[27] T. Gadzikwa, R. Bellini, H. L. Dekker, J. N. H. Reek, *J. Am. Chem. Soc.* **2012**, *134*, 2860–2863.
[28] W. M. Hart-Cooper, K. N. Clary, F. D. Toste, R. G. Bergman, K. N. Raymond, *J. Am. Chem. Soc.* **2012**, *134*, 17873–17876.
[29] W. M. Hart-Cooper, C. Zhao, R. M. Triano, P. Yaghoubi, H. L. Ozores, K. N. Burford, F. D. Toste, R. G. Bergman, K. N. Raymond, *Chem. Sci.* **2015**, *6*, 1383–1393.
[30] C. J. Hastings, D. Fiedler, R. G. Bergman, K. N. Raymond, *J. Am. Chem. Soc.* **2008**, *130*, 10977–10983.
[31] C. He, J. Wang, L. Zhao, T. Liu, J. Zhang, C. Duan, *Chem. Commun.* **2013**, *49*, 627–629.
[32] D. H. Leung, D. Fiedler, R. G. Bergman, K. N. Raymond, *Angew. Chem.* **2004**, *116*, 981–984.
[33] T. Murase, S. Horiuchi, M. Fujita, *J. Am. Chem. Soc.* **2010**, *132*, 2866–2867.
[34] B. Olenyuk, J. A. Whiteford, A. Fechtenkötter, P. J. Stang, *Nature* **1999**, *398*, 796–799.
[35] D. Pluth Michael, G. Bergman Robert, N. Raymond Kenneth, *Science* **2007**, *316*, 85–88.
[36] Y. Qiao, L. Zhang, J. Li, W. Lin, Z. Wang, *Angew. Chem. Int. Ed.* **2016**, *55*, 12778–12782; *Angew. Chem.* **2016**, *128*, 12970–12974.
[37] Y. Ueda, H. Ito, D. Fujita, M. Fujita, *J. Am. Chem. Soc.* **2017**, *139*, 6090–6093.
[38] M. Yoshizawa, M. Tamura, M. Fujita, *Science* **2006**, *312*, 251–254.

[39] Y. Fang, Z. Xiao, A. Kirchon, J. Li, F. Jin, T. Togo, L. Zhang, C. Zhu, H.-C. Zhou, *Chem. Sci.* **2019**, *10*, 3529–3534.
[40] J. Guo, Y. W. Xu, K. Li, L. M. Xiao, S. Chen, K. Wu, X. D. Chen, Y. Z. Fan, J. M. Liu, C. Y. Su, *Angew. Chem. Int. Ed.* **2017**, *56*, 3852–3856; *Angew. Chem.* **2017**, *129*, 3910–3914.
[41] G. Liu, Z. Ju, D. Yuan, M. Hong, *Inorg. Chem.* **2013**, *52*, 13815–13817.
[42] M. Sun, C. Sun, X. Wang, Z. Su, *Catal. Commun.* **2020**, *137*, 105930.
[43] J. Jiao, C. Tan, Z. Li, Y. Liu, X. Han, Y. Cui, *J. Am. Chem. Soc.* **2018**, *140*, 2251–2259.
[44] Y.-H. Zou, Q.-J. Wu, Q. Yin, Y.-B. Huang, R. Cao, *Inorg. Chem.* **2021**, *60*, 2112–2116.
[45] S. Lee, J. H. Lee, J. C. Kim, S. Lee, S. K. Kwak, W. Choe, *ACS Appl. Mater. Interfaces* **2018**, *10*, 8685–8691.
[46] J. Liu, W. Duan, J. Song, X. Guo, Z. Wang, X. Shi, J. Liang, J. Wang, P. Cheng, Y. Chen, M. J. Zaworotko, Z. Zhang, *J. Am. Chem. Soc.* **2019**, *141*, 12064–12070.
[47] J. Dong, Y. Pan, H. Wang, K. Yang, L. Liu, Z. Qiao, Y. D. Yuan, S. B. Peh, J. Zhang, L. Shi, H. Liang, Y. Han, X. Li, J. Jiang, B. Liu, D. Zhao, *Angew. Chem. Int. Ed.* **2020**, *59*, 10151–10159; *Angew. Chem.* **2020**, *132*, 10237–10245.
[48] N. Xu, Y.-X. Tan, E. I. S. M. El-Sayed, D. Yuan, *Cryst. Growth Des.* **2022**, *22*, 2768–2773.
[49] H. Wang, N. T. Jui, *J. Am. Chem. Soc.* **2018**, *140*, 163–166.
[50] S. Daliran, M. Khajeh, A. R. Oveisi, J. Albero, H. García, *ACS Appl. Mater. Interfaces* **2022**, *14*, 36515–36526.
[51] Z. Guo, X. Liu, Y. Che, D. Chen, H. Xing, *Inorg. Chem.* **2022**, *61*, 2695–2705.
[52] X. Liu, Z. Guo, Y. Che, R. Bai, Y. Chi, C. Guo, H. Xing, *ACS Appl. Mater. Interfaces* **2021**, *13*, 34114–34123.

Manuscript received: September 22, 2022
Accepted manuscript online: October 12, 2022
Version of record online: November 9, 2022